BROOKHAVEN
NATIONAL LABORATORY

BNL-79910-2008-CP

Dipole magnet for use of RHIC EBIS HEBT line

Takeshi Kanesue
Kyushu University, Fukuoka 819-0395, Japan

Masahiro Okamura, John Ritter, Deepak Raparia
BNL, Upton, NY 11973, USA

Presented at the 11th Biennial European Particle Accelerator Conference (EPAC 2008)
Genoa, Italy
June 23-27, 2008

Collider-Accelerator Department

Brookhaven National Laboratory
P.O. Box 5000
Upton, NY 11973-5000
www.bnl.gov

DISCLAIMER

DIPOLE MAGNET FOR USE OF RHIC EBIS HEBT LINE

Takeshi kanesue, Kyushu University, Fukuoka 819-0395, Japan
Masahiro Okamura, John Ritter, Deepak Raparia, BNL, Upton, NY 11973, U.S.A.

Abstract

Construction and magnetic field measurement of dipole magnets for RHIC-EBIS HEBT line have completed. These magnets will be used to guide highly charged ion beams ranging from proton to Uranium provided by a new injector toward the Booster ring in BNL. In this paper, overview of the magnetic design of the dipoles and results of magnetic field measurement are summarized.

INTRODUCTION

RHIC-EBIS is a new pre-injector for RHIC and for NASA Space Radiation Laboratory being built at Brookhaven National Laboratory (BNL), which will provide various ions from proton to Uranium [1]. The ions are accelerated to 2 MeV / amu by an RFQ and an IH linac before a HEBT bending section. In the HEBIT section, two identical H type dipole magnets provide total of 145.8 degrees bend (72.9 degrees of each) with a 1.3 m radius to guide radius to the Booster. Because its operation range is wide from 0.157 T to 0.964 T, a special attention was paid in the design process to cover the range. Variations of effective length and multipole components of the field were optimized to reduce as low as possible. There is a penetrating hole on the outer side wall of the magnet for an existing beam line coming from Tandem Van de Graaffs injector and the effect of this hole was also taken into account in the simulation. These magnets are required to change the field strength within a second according to demanded ion species. Table 1 shows the requirements for these magnets where the effective length is derived from the integrated field along the orbit and a field strength at the magnet center point.

Table 1 magnet specifications

gap height [cm]	13.54
operating range [T]	0.157-0.964
bend radius [m]	1.3
bend angle [degree]	72.9
useful aperture [cm]	5.0
effective length [cm]	165.32

MAGNET DESIGN

Figure 1 shows a schematic view of the magnet. These magnets were machined out from rectangular blocks made of stacked 1 mm laminated steel plates. The stacking direction is perpendicular to beam axis at the center of the magnet. There are no edge angles at both sides of the magnet. TOSCA code [2] was used for the design filed optimization. Conductor currents corresponding to He^{2+} and Au^{32+} were assumed in the optimization. The gap full height is 13.54 cm. At the both end of the magnet, edge chamfers were machined by 95 mm x 95 mm with 45 degrees cutting angle. These are determined to minimize the effective length variation caused by the saturation effect of the iron. With this chamfer cuts, the difference was reduced to 3.3 mm which corresponds to 0.20 % of the required effective length. There are bumps of which height is 2.3 mm at both sides of the magnet pole face. These shimmed shapes and location were optimized to reduce the integrals of the multipole components on the circle perpendicular to the reference orbit direction, which is the ideal beam trajectory, with reference radius of 5 cm. The quadrupole component of the field was adjusted by changing the ratio of the widths of the two bumps, the inner and the outer. Then sextupole component was optimized by changing the widths keeping the same ratio.

We found the multipole components can be reasonably corrected except octupole which is caused by an asymmetric condition of the magnet's cross section. A slight weak field area was found at inner side of the magnet near poles. We decided to add another small bump to correct this effect which reduces about 6 units of the integrated octupole component. The bump has a shape of 5 mm width and 0.8 mm height as seen in Fig. 2. Table 2 shows the final performance calculated by TOSCA.

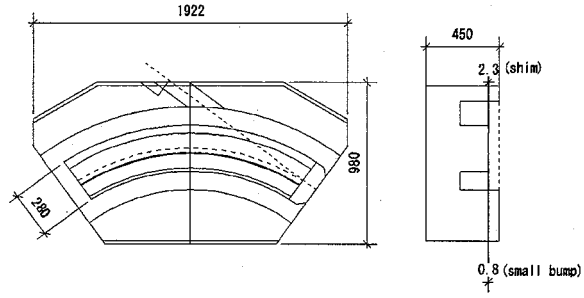

Figure 1: Schematic view of dipole magnet.

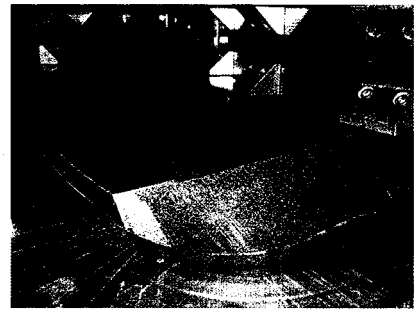

Figure 2: Pole shape with the bumps. A small bump along the orbit which corrects octupole component of the field can be seen at the circled point.

Work performed under contract No. DE-AC02-98CH10886 under the auspices of the United States DOE

Table 2: Designed dipole magnet performance calculated by TOSCA. Multipole components are the integrated value along the reference radius of 5 cm and are expressed in "unit," which is 1/10000 of main dipole field.

	B at center (Gauss)	effective length (cm)	Quadrupole	Sextupole	Octupole
Full current	9643	165.18	-11.25	-7.58	-0.44
He current	3146	165.51	-12.65	4.00	2.57
effective length variation		3.3mm (0.2 %)			

MAGNETIC FIELD MEASUREMENT

The fabrication and the magnetic field measurements were done by SIGMAPHI in Vannes, France. Figure 3 shows one of the completed magnets. In the measurements, a Hall probe was attached to an automated displacement table controlled by servo motors. The position of the probe was adjusted reference to some alignment pins those will be used for installation of the magnet. The field strength on the median plane were scanned along to the bending curvatures, R = 1300 mm (reference orbit), R = 1350 mm and R = 1250 mm. Four currents, 2250 A, 1687.5 A, 1125 A and 562.5 A, were tested for the each magnet. In this report, to simplify the discussion, only the half measured data (from the right side of the magnet in Fig. 1) of the firstly produced magnet is used, since both measurements gave similar and almost symmetric results. The effect of the hole at the outer side was also investigated, however obvious asymmetry field shape was not observed near the beam path as expected.

The magnetic field strength at the center of the magnet with 2250 A was 0.9956 T which is in good agreement to 0.9924 T calculated by TOSCA. Figure 4 shows the measured and the predicted magnetic field strengths along the radii starting from the center of the magnet. The all calculated values were normalized by the field strength at the magnet center on the 1300 mm radius for clear comparison. At the center of the magnet the outer and the inner sides of the fields were measured slightly lower than expectations. Those discrepancies might be caused by the coil position in the 3D model, assumed B-H property of the iron and reinforced iron plates of the outer surface of the real magnets.

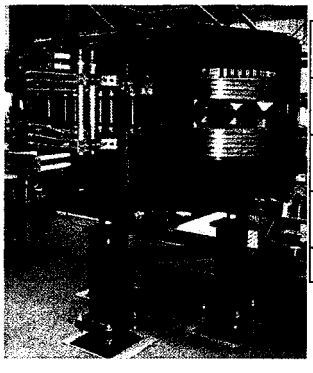

main coil current	2250A
trim coil current	45A
water flow	126 L/min
operation pressure	10Bar
total weight	10500 kg

Figure3: The fabricated dipole magnet on a stand and magnet technical data

Figure 5 shows the effective lengths as a function of the currents. The behaviors of the two curves are almost identical. This means the 45 degrees straight chamfer cut works as expected. The measured effective length is about 7 mm longer than the prediction; however slight field distribution difference at inside region of the magnet makes large discrepancy since the length is normalized by the field strength at the center point. At the fringe area, the difference is about 2 mm each. The sensing area of the probe is 1 x 1 mm and this discrepancy seems within a reasonable range.

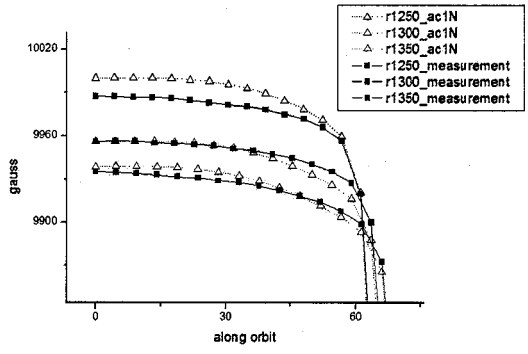

Figure 4: The measured and the predicted magnetic field strengths along the radii.

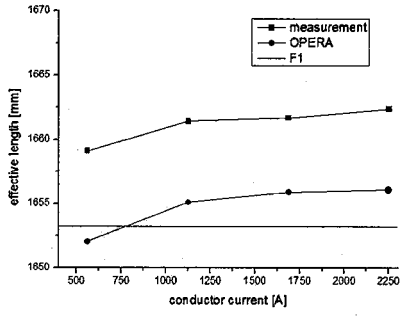

Figure 5: The effective length as a function of a current.

MULTIPOLE ANALYSIS

Since the fields on the off cantered radii, r = 1250 and 1350 mm, are lower than we expected, we tried to evaluate multipole components along the reference orbit, using the measured simple data. We can derive quadrupole and sextupole components from three

measured points, r = 1250, 1300 and 1350 mm, by applying quadratic fitting;

$$. B = C_0 + C_1 X + C_2 X^2$$

Here constants, C_0, C_1 and C_2 are dipole, quadrupole and sextupole components, respectively. The B is the field distribution and three points of coordinates, -5, 0, +5 are input to X, since the reference radius was assumed as 5 cm. In this fitting, all the higher multipoles are included in these three coefficients. For instance, the C_1 mainly indicates the amplitude of quadrupole component, however also includes octupole, decapole, and higher components. When we estimate the multipoles using the TOSCA, we usually took more than a hundred points along the reference circle around the central orbit. In this case, the Fourier integration gives relatively purer multipole values. And also, the simulation gives three measured point fields which can be applied to the quadratic fitting. In the simulation, it is easy to extract the effects of the higher order multipole effects from the quadratic coefficients. So by subtracting the numerically derived the effects of the higher multipoles from the measured coefficents, we can assume more realistic quadrapole and sextupole components. By applying the process mentioned above, the estimated quadrupole and sextupole component based on the measurements are -16.3 and 10.0 unit.

CONCLUSION

The HEBIT dipole magnets for the RHIC-EBIS project were fabricated and the field measurements were finished. The measured fields agreed well to the numerical simulation results. The effective length variation due to the various field excitations was minimized and was verified by the measurement. The integrated multipole components along the beam path were estimated from the simple data set obtained by the measurements. The estimated quadrupole and sextupole component were -16.3 and 10.0 unit, respectively. All the specifications matched to our requirements.

ACKNOWLEDGEMENT

The mechanical design work, fabrication and the field measurements were done by SIGMAPHI. We thank them about good collaboration with us.

REFERENCES

[1] J. Alessi, et. al., "HIGH PERFORMANCE EBIS FOR RHIC", PAC07, Albuquerque, 2007, p3782.
[2] Vector Fields Ltd, Oxford, UK

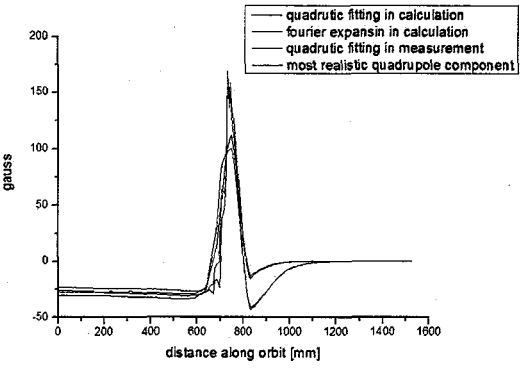

Figure 6: Quadrupole component distribution derived from quadratic fitting using TOSCA (black), fourier expansion using TOSCA (red), quadratic fitting using measured data (green) and most realistic quadruple component which was obtained by subtracting the effect of higher multipoles from green data set.

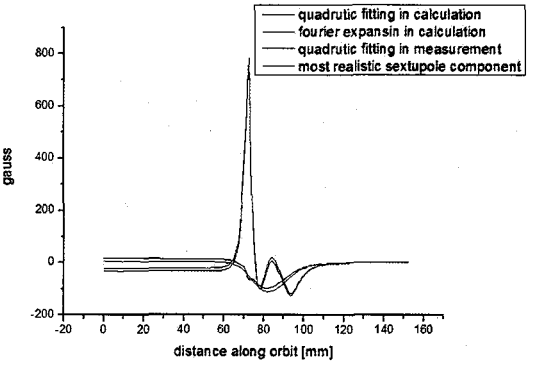

Figure 7: Sextupole component distribution derived from quadratic fitting using TOSCA (black), fourier expansion using TOSCA (red), quadratic fitting using measured data (green) and most realistic sextupole component which was obtained by subtracting the effect of higher multipoles from green data set.